

On the Dynamics and Structure of Three-Dimensional Trans-Alfvénic Jets

Philip E. Hardee and Alexander Rosen

Department of Physics & Astronomy

The University of Alabama

Tuscaloosa, AL 35487

hardee@athena.astr.ua.edu, rosen@eclipse.astr.ua.edu

ABSTRACT

Three-dimensional magnetohydrodynamical simulations of strongly magnetized “light” conical jets have been performed. An investigation of the transition from sub-Alfvénic to super-Alfvénic flow has been made for nearly poloidal and for helical magnetic fields. The jets are stable to asymmetric modes of jet distortion provided they are sub-Alfvénic over most of their interior but destabilize rapidly when they become on average super-Alfvénic. The jets are precessed at the origin and the resulting small amplitude azimuthal motion is communicated down the jet to the Alfvén point where it couples to a slowly moving and rapidly growing helical twist. Significant jet rotation can contribute to destabilization via increase in the velocity shear between the jet and the external medium. Destabilization is accompanied by significant mass entrainment and the jets slow down significantly as denser external material is entrained. Synchrotron intensity images satisfactorily reveal large scale helical structures but have trouble distinguishing a large amplitude elliptical jet distortion that appears as an apparent pinching in an intensity image. Smaller scale jet distortions are not clearly revealed in intensity images, largely as a result of the relatively small total pressure variations that accompany destabilization and growing distortions. Fractional polarization is high as a result of the strong ordered magnetic fields except where the intensity image suggests cancellation of polarization vectors by integration through twisted structures.

Subject headings: galaxies: jets — hydrodynamics — instabilities — MHD

1. Introduction

Highly collimated outflows are observed to emanate from the centers of galaxies and quasars, from neutron star and black hole binary star systems, and from protostellar systems. Hydrodynamic jet models can account for many aspects of the dynamics and morphology of the extended jets – both galactic and extragalactic. However, simple flux conservation arguments imply and recent jet acceleration and collimation schemes require dynamically strong magnetic

fields close to the central engine. Numerical studies, e.g., Meier, Payne, & Lind (1996); Ouyed, Pudritz, & Stone (1997); Ouyed & Pudritz (1997); Romanova et al. (1997), show that the jets created in this fashion pass through slow magnetosonic, Alfvénic, and fast magnetosonic critical points. The ultimate jet velocity may depend on the configuration of the magnetic field (Meier et al. 1997), and the jets accelerate up to asymptotic speeds that may be only a few times the Alfvén speed at the Alfvén point – at the Alfvén point the jet speed equals the Alfvén speed (Camenzind 1997). This basic acceleration and collimation process may be the same for all classes of objects that emit jets (Livio 1997).

Highly collimated flows are susceptible to Kelvin-Helmholtz (K-H) or current driven (CD) instabilities. The K-H instability of three-dimensional (3D) jets with purely poloidal or purely toroidal magnetic fields (Ray 1981; Ferrari, Trussoni, & Zaninetti 1981; Fiedler & Jones 1984; Bodo et al. 1989), and of jets containing force-free helical magnetic fields (Appl & Camenzind 1992; Appl 1996) has been extensively investigated. Additional investigations have considered the potential role of current driven pinching of toroidally magnetized columns (Begelman 1998). At least for force-free helical magnetic fields it appears that the K-H instability exhibits faster growth and is more likely to be responsible for producing asymmetric structure than current driven instability (Appl 1996). In general, spatial or temporal growth rates associated with the K-H instability are found to increase as the magnetosonic Mach number decreases provided the jet is super-Alfvénic. Unlike purely fluid flows which are unstable when subsonic, the poloidally magnetized jet is predicted to be nearly completely stabilized to the K-H instability when the jet is sub-Alfvénic. Additionally, an appropriately configured dynamically significant magnetic field may have a stabilizing influence on the super-Alfvénic jet. Nevertheless, the fact that magnetically accelerated and collimated jets must pass through a super-Alfvénic but transmagnetosonic region implies a potential zone of enhanced instability just downstream of the Alfvén point.

Previous numerical work designed to investigate the effect of strong magnetic fields on jet stability (Hardee et al. 1992; Hardee & Clarke 1995) were conducted using two dimensional (2D) slab jet geometry. A slab jet is spatially resolved along two Cartesian axes and is effectively infinite in extent in the third dimension. The 2D nature of such simulations reduced computer memory and CPU requirements. A theoretical analysis of the stability properties of the slab jet reveals that the jet is K-H unstable to a symmetric pinching mode and an asymmetric sinusoidal mode that provide reasonable analogs to the pinching and helical twisting of a 3D jet. The numerical simulations confirmed that the stability properties of the axially magnetized slab jet behaved according to predictions made by a stability analysis. In particular, it was demonstrated that a super-Alfvénic jet becomes more stable as the magnetosonic Mach number increases with a destabilization length varying approximately proportional to the magnetosonic Mach number. The slab jet simulations showed a complete stabilization of the jet to sinusoidal distortion when the jet was sub-Alfvénic, and showed the predicted rapid destabilization at the Alfvén point where the flow becomes super-Alfvénic but is transmagnetosonic. The numerical simulations also showed that magnetic tension can significantly modify the development of instability in the nonlinear

regime and in 2D prevent disruption of the flow. However, the 2D slab jet has no analog to the higher order modes of distortion (elliptical, triangular, rectangular, etc.) of the 3D jet. These modes make the 3D jet more unstable than the 2D slab jet and lead to enhanced spatial mass entrainment rates (cf., Rosen et al. 1999, hereafter RHCJ). Momentum and mass exchange with an external environment more dense than the jet results in relatively rapid loss of the initial high collimation, and the outwards flow broadens and slows as denser external material is heated, mixed with, and accelerated by the lighter jet fluid. Thus, it is of considerable interest to see the effect of very strong magnetic fields on mass entrainment in 3D. Additionally, it is of interest to ascertain the types of jet structures arising near the Alfvén point, and to search for a connection between these structures and observed jet structures.

It is our purpose here to begin a numerical investigation of the dynamical and stability properties of strongly magnetized flows in 3D. Ultimately we hope to shed some light on the structures associated with magnetized jet configurations near the jet acceleration and collimation region, and to provide some connection between the acceleration and collimation region and observed jet structures on larger spatial scales. In this paper we analyze results from 3D simulations designed to study the predicted rapid destabilization at the transition between sub-Alfvénic and super-Alfvénic flow and to study the effect of strong fields on mass entrainment. In §2 the numerical setup and results of the numerical simulations are presented. The simulations are initialized by establishing a cylindrical helically magnetized jet across a computational grid in an unmagnetized surrounding medium with pressure gradient devised to result in a constant expansion of the jet once pressure equilibrium is achieved. Thus, these simulations are relevant to astrophysical jets far behind the propagating jet head and in an assumed quasi-steady state region. Total synchrotron intensity images and fractional polarization vectors provide a connection between jet dynamics and potentially observable jet structures in extragalactic jets, and also provide some insight into potential structures in radiatively cooled protostellar or Seyfert jets. In §3 the structures expected to arise as a result of the K-H instability are presented and compared to structures appearing in the numerical simulations. Finally, in §4 we summarize our results and discuss some of the implications for astrophysical jets.

2. Numerical Simulations

2.1. Initialization

Simulations were performed using the three dimensional MHD code ZEUS-3D, an Eulerian finite-difference code using the Consistent Method of Characteristics (CMoC) which solves the transverse momentum transport and magnetic induction equations simultaneously and in a *planar split* fashion (Clarke 1996). Interpolations were carried out by a second-order accurate monotonic upwinded time-centered scheme (van Leer 1977) and a von-Neumann Richtmyer artificial viscosity was used to stabilize shocks. The code has been thoroughly tested via MHD test suites as

described by Stone et al. (1992) and Clarke (1996) to establish the reliability of the techniques.

All simulations are initialized by establishing a cylindrical jet across a 3D Cartesian grid resolved into $130 \times 130 \times 370$ zones. With this grid the simulations required about 126 Mwords of memory on the Cray C90 at the Pittsburgh Supercomputer Center. Thirty uniform zones span the initial jet diameter, $2R_0$, along the transverse Cartesian axes (x -axis and y -axis). Outside the uniform grid zones, the zones are ratioed where each subsequent zone increases in size by a factor 1.05. Altogether the 130 zones along the transverse Cartesian axes span a total distance of $30R_0$. Along the z -axis 280 uniform zones span a distance of $40R_0$ outwards from the jet origin. An additional 90 ratioed zones span an additional distance of $40R_0$ where each subsequent zone increases in size by a factor 1.02. Altogether the 370 zones along the z -axis span a total distance of $80R_0$. Outflow boundary conditions are used except where the jet enters the grid where inflow boundary conditions are used. The use of a non-uniform grid such as we are employing has been shown to have the beneficial effect of reducing reflections off the grid boundaries as a result of increased dissipation of disturbances (Bodo et al. 1995).

The jets are initialized across the computational grid with a uniform density ρ_{jt} and initial radius R_0 . The magnetic field in the jet is initialized with a uniform axial component, B_z , and a toroidal magnetic component with functional form $B_\phi = B_\phi^{pk} \sin^2[\pi f(r)]$ where for $r < r_{pk}$, $f(r) = 0.5(r/r_{pk})^a$, and for $r_{pk} < r < r_{\max}$, $f(r) = 1.0 - 0.5[(1 - r/r_{\max})/(1 - r_{pk}/r_{\max})]^b$. In these simulations the toroidal component increases to a maximum, B_ϕ^{pk} , at $r_{pk} = 0.5R_0$, and declines to zero at $r_{\max} = 0.9R_0$ so that initially all currents flow within the jet. This particular toroidal profile is not physically motivated but with $a = b = 0.315$ provides a broad cross sectional region within the jet in which the toroidal magnetic component is relatively constant (nearly constant helical pitch, plasma beta, and magnetosonic speed) and also is well behaved numerically. In the external medium the magnetic field is equal to zero. The equation of hydromagnetic equilibrium

$$\frac{d}{dr} \left(p_{jt}(r) + \frac{B_z^2(r)}{8\pi} + \frac{B_\phi^2(r)}{8\pi} \right) = -\frac{B_\phi^2(r)}{4\pi r},$$

where the term on the right hand side describes the effects of magnetic tension, has been used to establish a suitable radial gas pressure profile in the jet by varying the jet temperature. The sonic, Alfvénic and magnetosonic Mach numbers in the jet are $M_{jt}(r) \equiv u/a_{jt}(r)$, $M_A(r) \equiv u/V_A(r)$ and $M_{ms}(r) \equiv u/a_{ms}(r)$ where $a_{jt}^2(r) = \Gamma p(r)/\rho_{jt}$, $\Gamma = 5/3$, $V_A^2(r) = B^2(r)/4\pi\rho_{jt}$, and we define a jet magnetosonic speed as $a_{ms}(r) \equiv (a_{jt}^2 + V_A^2)^{1/2}$. We categorize simulations by the magnetosonic Mach number on the jet axis but note that the dynamics can depend on details of the magnetic and temperature profiles. Since internal dynamics and timescales involve wave propagation across a jet with sound, Alfvén and magnetosonic speeds which are a function of jet radius, we can define radial averages as, for example,

$$\langle M_{ms} \rangle \equiv \frac{1}{R_{jt}} \int_0^{R_{jt}} M_{ms}(r) dr$$

that will differ for different magnetic, density and temperature profiles.

In the simulations the external medium is isothermal and the external density, $\rho_{ex}(z)$, declines to produce a pressure gradient, $p_{ex}(z) \propto \rho_{ex}(z)$, that is designed to lead to a constant expansion, $R_{jt}(z) = (1 + z/80R_0)R_0$, of a constant velocity adiabatic jet containing uniform poloidal magnetic field and an internal toroidal magnetic field that provides some confinement, i.e.,

$$\rho_{ex}(z) = \frac{[(R_{jt}/R_0)^{-10/3} + C_p(R_{jt}/R_0)^{-4} - C_\phi(R_{jt}/R_0)^{-2}]}{[1 + C_p - C_\phi]} \rho_{ex}(0) .$$

The values of C_p and C_ϕ depend on the poloidal and toroidal field strengths, and the ratio of the magnetic pressure relative to the thermal pressure. The jet speed is initialized so that the jets are sub-Alfvénic initially, but after expansion to achieve pressure equilibrium with the external medium cross the Alfvén and fast magnetosonic points on the computational grid. All jets are initialized with a velocity $u = 4a_{ex}$ and a density $\rho_{jt} = 0.029\rho_{ex}(0)$. The jet sound, Alfvén, and magnetosonic speeds at jet center normalized to the external sound speed; radial averages of the jet sonic, Alfvénic, and magnetosonic Mach numbers at the inlet, and values of C_p and C_ϕ for the simulations are given in Table 1. Absolute values for jet speed, density, temperature, and magnetic field strength are completely determined by choosing values for the external density, $\rho_{ex}(0)$, and the external temperature, T_{ex} , or sound speed, a_{ex} . An absolute length scale is determined by choosing a value for R_0 .

Simulations A and B contain a primarily poloidal magnetic field with only a weak toroidal component, $B_\phi^{pk}/B_z \sim$ (A) 0.086 & (B) 0.05 at the inlet, so as to be directly comparable to predictions made by a linear stability analysis (§3). In addition, jet parameters in simulation A at the inlet are very nearly identical to jet parameters in a 2D MHD expanding slab jet simulation (Hardee & Clarke 1995). In simulation B the poloidal and toroidal magnetic field strengths are reduced and the jet thermal pressure is increased relative to simulation A. In simulation B the Alfvén and magnetosonic points move closer to the inlet. Simulations C & D contain a poloidal magnetic field that is the same as in simulation B but now the toroidal component $B_\phi^{pk}/B_z \sim 0.44$ at the inlet. The thermal pressure and toroidal magnetic field radial profiles used in the four simulations are shown in Figure 1. The total magnetic field strength in simulations C & D has been designed to be comparable to the total magnetic field strength in simulation A at an axial distance of $z = 40R_0$. If constant adiabatic expansion and velocity, along with decline in the jet density and poloidal magnetic field proportional to R_{jt}^{-2} are assumed, then the Alfvén point evaluated on the jet axis where the toroidal component of the magnetic field is zero would occur at axial distances of (A) $40R_0$ and (B, C & D) $20R_0$.

In all simulations the jet is driven by a periodic precession of the jet velocity, u , at an angle of 0.01 radian relative to the z -axis with an angular frequency $\omega = 0.5a_{ex}/R_0$. The initial transverse motion imparted to the jet by this precession is well within the linear regime. The precession serves to break the symmetry and the precessional frequency is chosen to be below the theoretically predicted maximally unstable frequency associated with helical twisting of a K-H unstable supermagnetosonic jet with jet radius $R_{jt} \geq R_0$. In simulations A, B and C the precession is in a counterclockwise sense when viewed outwards from the inlet. This direction

of precession induces a helical twist in the same sense as that of the magnetic field helicity and helical wavefronts are at shallow angles to the helically twisted magnetic field lines. In simulation D the precession is clockwise and helical wavefronts associated with the precessional motion will be at larger angles relative to the helically twisted magnetic field lines.

2.2. Simulation Results

In all simulations the jets expand rapidly, and after about five dynamical times, $\tau_d \equiv (a_{ex}/R_0)t \approx 5$, have achieved an approximate static pressure equilibrium with the surrounding medium. In all cases the jets achieve a nearly constant expansion rate on the computational grid with $R_{jt} \approx 2R_0$ when $z = 80R_0$. After dynamical times $\tau_d =$ (A) 68, (B) 56, and (C & D) 44 the numerical simulations have reached a quasi-steady state out to axial distances between $45R_0$ and $60R_0$ depending on the simulation. The dynamical times correspond to ~ 3.5 precessional periods and ~ 3.5 flow through times through an axial distance of $50R_0$ in simulations C & D and correspondingly more precessional periods and flow through times in simulations A & B. The simulations were terminated before a quasi-steady state was achieved across the entire computational grid because excessive CPU time would have been required. The simulations required (A) 200, (B) 160, and (C & D) 360 CPU hours on the Cray C90 at the Pittsburgh Supercomputer Center.

Plots of the velocity components along the z -axis shown in Figure 2 reveal that the jets accelerate in response to the magnetic and thermal pressure gradients. In simulations A & B with primarily poloidal magnetic fields the jets accelerate up to some asymptotic speed early in the simulation but do not quite reach the initial asymptotic speed at later dynamical times as they are slowed by the onset of instability. Instability is manifested by the rapid growth in the amplitude and by the oscillation of the transverse velocity components, and by the fluctuation and decline in the axial velocity. Significant fluctuation in axial and transverse velocity components begins at an axial distance of (A) $\sim 40R_0$ and (B) $\sim 20R_0$. In simulations A & B transverse velocities are less than 2% of the jet speed inside the destabilization point but grow to values as large as (A) 35% and (B) 40% of the jet speed shortly after destabilization. Transverse velocity oscillations with scale lengths $\lambda_h \sim$ (A) $7.6R_0$ and (B) $7.1R_0$ are out of phase in the orthogonal transverse directions suggesting a 3D “helical” distortion, and not, for example, a 2D “sinusoidal” distortion of the jet beam. Fluctuations in the axial velocity are the result of the jet flow being displaced off the z -axis.

More acceleration is evident in simulations C & D than in simulation B. Recall that the poloidal magnetic field is the same in simulations B, C & D. Nevertheless simulations C & D show the same basic initial behavior as simulations A & B, i.e., jet acceleration up to some asymptotic speed early in the simulation followed by development of instability at later dynamical times. Instability occurs somewhat closer to the inlet in simulations C & D than in simulation B. Note an indication of relatively large transverse velocities immediately outside the inlet, up to 10% of

the jet speed near to the jet axis, which decrease but then become as large as 35% of the jet speed as the jets destabilize. The initial large transverse motions are indicative of jet rotation in these two simulations, and occur as the code modifies the initial input static equilibrium state to an appropriate dynamic equilibrium state, i.e., $\nabla \times (\mathbf{u} \times \mathbf{B}) = 0$. We note that dynamic equilibrium is achieved across the computational grid as the jets expand to achieve static pressure balance with the external medium. We also note that dynamic equilibrium is achieved throughout the duration of the simulation within one jet radius of the inlet. The jet rotational speed is on the order of the external sound speed and is about 25% of the initial jet speed. In these two simulations this azimuthal motion is vastly larger than the azimuthal motion induced at the inlet by the precession. Simulations C & D show significant fluctuation in axial and transverse velocity components associated with instability beginning at an axial distance of $\sim 15R_0$. Major transverse velocity oscillations with scale length $\lambda_h \sim 6.5R_0$ (not too different from simulation B) are complicated by other smaller scale features but indicate helical motion of the jet beam. In simulations C & D more rapid and larger amplitude fluctuation is seen in the axial velocity than in simulations A & B.

Plots of the axial velocity along with the sonic, Alfvénic, and magnetosonic speeds along the z -axis including the Alfvén and fast magnetosonic points and plots of transverse structure along the x -axis between the Alfvén and fast magnetosonic points are shown in Figure 3. Jet acceleration downstream of the inlet results in Alfvén and fast magnetosonic points on the z -axis at distances $z_A \sim$ (A) $37R_0$, (B) $8R_0$, (C) $6R_0$, and (D) $8R_0$, and $z_{ms} \sim$ (A) $42R_0$, and (B, C & D) $20R_0 - 24R_0$, respectively. The choice of a cut point just downstream of the Alfvén point on the jet axis reveals the relatively undisturbed jet profile before significant instability appears. The transverse profile is particularly important as the jet may still remain sub-Alfvénic off the axis and stable. The plots of transverse structure show that the poloidally magnetized jets in simulations A & B have relatively flat (top hat) density, temperature, and magnetic field strength and velocity profiles, while the helically magnetized jets in simulations C & D show considerably more transverse structure. The jets can become super-Alfvénic off the jet axis at a significantly different point than on the jet axis, and, for example, the average Alfvénic Mach number $\langle M_A \rangle \approx 1$ at an axial distance $\langle z_A \rangle \sim$ (A) $35R_0$, (B) $8R_0$, and (C & D) $14R_0$. In simulation A a small enhancement in the Alfvén speed on the jet axis leaves the jet sub-Alfvénic on the axis while already super-Alfvénic off the axis. The helically magnetized jets in simulations C & D become super-Alfvénic on the jet axis and at the jet surface where the toroidal component of the magnetic field is zero while remaining sub-Alfvénic in much of the jet interior. Note that in simulations C & D the Alfvén speed in the jet interior is as much as 9% higher than on the jet axis but the total jet speed including rotation is only about 3% higher than on the jet axis. In all simulations the jets remain stable to large scale velocity fluctuations at the jet center until they become on average super-Alfvénic. Significant large scale velocity fluctuations develop before the jet can become supermagnetosonic.

The mass entrained by the jets, and the average velocity of jet plus “entrained” material in

the four simulations are plotted in Figure 4. In particular, we define the mass per unit length, $\sigma(z)$, at any point along the jet as $\sigma = \int_A f \rho dy dx$, where A is the cross sectional area of the computational domain at axial position z , and f is set to 1 if the local magnetic field is above 4% of the expected maximum field strength along the jet at z [$B(z) > 0.04B_{jt,max}(z)$], and f is set to 0 otherwise. We define the entrained mass by the presence of a magnetic field since only the jet material is initially magnetized. The setting of f to 1 or 0 effectively assumes that zones with any fraction of jet material, as defined by the presence of magnetic field, are considered mixed with the external medium in that zone. This technique provides results similar to estimating mass entrainment by using a threshold axial velocity (RHCJ). Setting the switch at a magnetic field strength of 4% of the expected maximum strength at z reduces the effects of numerical diffusion, and also reduces the sensitivity of the value of σ to a small diffusion of the field into the external medium which is much denser than the jet material. Even so there is a large increase in σ at the jet inlet. Simulations A and B provide a useful baseline value of $\sigma/\sigma_{jt} \approx 10$ (σ_{jt} is the expected value at the inlet) that could be the result of numerical diffusion. Thus, for example we might assume that a value of $\sigma/\sigma_{jt} = 20$ infers an entrained mass equal to the “initial” jet mass per unit length. We note that the high density in the external medium relative to the jet density at the inlet results in the observed value of σ at the inlet if the jet magnetic field promptly diffuses radially by about two computational zones. Note that the average velocity of “entrained” plus jet material is very low at the inlet in simulations A and B. If we also consider Figure 5 which shows gray scale axial velocity cross sections, we infer that dense material “entrained” near to the inlet is moving very slowly in a thin sheath around a rapidly moving jet core. The slow motion of sheath material, typically more than an order of magnitude less than the core speed, means that insufficient time has passed in the simulation for the majority of “entrained” material to have moved far downstream and most mass has been picked up relatively locally. For example, the noticeable slow decrease in “entrained” mass in simulation A out to $z \approx 42R_{jt}$ occurs because the jet density at larger distance is higher relative to the external density – recall the external medium is isothermal and in equilibrium with an expanding adiabatic magnetized jet, thus the external density falls faster than the expanding jet’s density – with result that mass at larger distance falling within the $B(z) > 0.04B_{jt,max}(z)$ criterion is a smaller fraction of the jet’s mass.

In simulations A & B the onset of significant mass entrainment occurs relatively abruptly at axial distances of (A) $42R_0$ and (B) $19R_0$ as large transverse velocities develop, and the average velocity of jet plus “entrained” material shows a significant decline beyond these points. The maximum value of the mass per unit length is $(\sigma/\sigma_{jt})^{\max} \approx$ (A) 14 and (B) 45. These values would imply an entrained mass of about 0.4 and 3.5 times the initial jet mass per unit length, respectively, if we assume $\sigma/\sigma_{jt} = 10$ is an appropriate baseline level. In simulations C & D mass entrainment begins at an axial distance of $\sim 6R_0$, possibly slightly before the jet becomes super-Alfvénic on average when only the axial velocity is considered. This mass entrainment begins even before significant transverse velocity fluctuations are apparent on the jet axis. In simulations C & D the maximum value of the mass per unit length is $(\sigma/\sigma_{jt})^{\max} \approx 55$. This value implies an entrained mass of about 4.5 times the initial jet mass per unit length if we

assume $\sigma/\sigma_{jt} = 10$ is an appropriate baseline level. While an accurate quantitative value for the amount of mass entrained cannot be determined from these simulations, we can conclude that significant mass entrainment occurs when the jets become super-Alfvénic on average. We have examined our simulations to see if significant forward momentum flux, σv_z^2 , is carried by “unmixed” external material, i.e., material with $B(z) < 0.04B_{jt,max}(z)$. We evaluate the momentum flux in the simulations for $15 < z/R_0 < 60$. At least approximately these minimum and maximum limits on z span the range beyond the initial jet acceleration region out to the quasi-steady state limit. In simulations A & B the “unmixed” material in this range carries $\lesssim 2\%$ & $\lesssim 5\%$ of the momentum flux, respectively. We note that acceleration has led to a total momentum flux in this range about 1.15 and 1.35 times higher than at the inlet in simulations A & B, respectively. In simulations C & D the “unmixed” material between $15 < z/R_0 < 30$ carries $\lesssim 6\%$ of the momentum flux and acceleration has led to a total momentum flux in this range about 1.25 times higher than at the inlet. From $30 < z/R_0 < 60$ in simulations C & D the “unmixed” material carries $\lesssim 15\%$ of the momentum flux and the total momentum flux is now only about 70% of that at the inlet. The reduction in total momentum flux in simulations C & D compared to simulation B at $15 < z/R_0 < 30$ is likely the result of an elliptical distortion that appears in simulations C & D at small z . While momentum imparted to the “unmixed” material is not insignificant, it is clear that the majority of the jet kinetic energy remains carried by the “mixed” material.

In the super-Alfvénic mass entraining region we note that decline in the mass entrained at large axial distances is a consequence of termination of the simulations before a quasi-steady state is achieved across the entire computational grid. Decline in the entrained mass and increase in the velocity of jet plus entrained mass at large distances suggests that simulations A & B have reached a quasi-steady state out to about $55R_0 - 60R_0$, and simulations C & D out to about $45R_0$. We note that the spatial mass entrainment rate after destabilization is less in simulation A relative to B. The spatial mass entrainment rate in simulations C & D is higher than in simulation B for $z \leq 25R_0$ but the entrained mass in simulation B becomes comparable to C & D for $25R_0 \leq z \leq 35R_0$. The entrained mass in simulation B continues to increase steadily out to $z \approx 40R_0$. In simulations C & D the entrained mass remains relatively constant for $25R_0 \leq z \leq 39R_0$ with a sudden jump in the mass entrained at $z \sim 39R_0$. The entrained mass in simulations B, C & D is comparable between $40R_0 - 50R_0$ and remains relatively constant over this interval. This may indicate saturation like that found in other simulations (Bodo et al. 1995; RHCJ) or in this case be an effect of insufficient computational and flow through time.

Jet axial velocity cross sections shown in Figure 5 illustrate development of the surface distortions that promote mixing and mass entrainment, and that can move the jet flow completely off the initial axis. Small scale surface distortions in simulations A & B have formed before the jets become super-Alfvénic on the axis. These jets become super-Alfvénic near to the jet surface first, partly as a result of prompt entrainment at the jet inlet which raises the jet density, lowers the magnetic field strength, and reduces the Alfvén speed near the jet surface. Clearly these small scale surface distortions do not lead to significant mass entrainment. In particular we note a

“rectangular” distortion in simulation A appearing in the panel at $z = 24R_0$ with an admixture of “elliptical” and “triangular” distortion evident in the panels at $z = 48R_0$ and $54R_0$. The “rectangular” distortion rotates through 90° in an axial distance of $\lambda_r \sim 18R_0$. Note that jet distortions in simulation A are still confined near to the jet surface even at axial distances of $50R_0$ and the entrained mass remains low. The jet in simulation B exhibits considerable structure that consists of a combination of helical, elliptical, triangular, and rectangular distortions. For example, the panels at $z = 18R_0$ and $24R_0$ show evidence for triangular and rectangular distortion plus helical displacement, and primarily triangular distortion plus helical displacement, respectively, and an elliptical distortion is apparent in the panel at $z = 42R_0$. The development of significant jet distortion at $z = 24R_0$ is coincident with significant mass entrainment. Note that the jet flow has moved completely off the z -axis in the panel at $z = 48R_0$ as a result of helical displacement. Shifting of the jet off the z -axis leads to the decrease in axial and transverse velocities seen in Figure 2 at large axial distances in simulation B. In both of these simulations the jets indicate a diminishing higher speed core within a growing more slowly moving sheath at large distances.

The jet axial velocity cross section show that simulations C & D develop similarly, but with significantly different behavior from simulations A & B. The cross sections show a surface elliptical distortion by an axial distance of $6R_0$ with a scale length for rotation through 180° of $\lambda_e \sim 8R_0$. The higher order surface corrugations that appeared in simulations A & B are suppressed in these simulations. Ultimately these jets appear to become hollow in the axial velocity cross section at axial distances of $\sim 40R_0$. This occurs close to the location of the sudden jump in entrained mass in these two simulations. In these two simulations we almost lose the higher speed jet core entirely at large distances. The gray scale cross sections indicate that significant momentum is carried by a comparably large transverse region in simulations B, C & D. We will consider jet cross section distortion along with accompanying pressure and velocity fluctuation in more detail in the next section.

In Figure 6 total synchrotron intensity images containing fractional polarization B-vectors (vectors indicating the magnetic field direction) formed by line-of-sight integrations through the computational domain reveal the types of observational structures that might appear downstream of the Alfvén point. To some extent these images also reveal the extent of jet spreading as only the jet fluid is magnetized. To generate these images a synchrotron emissivity is defined by $p_{jt}(B \sin \theta)^{3/2}$ where θ is the angle made by the magnetic field with respect to the line of sight, and the simulated intensity and fractional polarization B-vectors are formed from the Stokes parameters. This emissivity mimics synchrotron emission from a system in which the energy and number densities of the relativistic particles are proportional to the energy and number densities of the thermal fluid. This simplistic assumption is necessary when the relativistic particles are not explicitly tracked (Clarke, Norman, & Burns 1989). While not designed to be comparable to line emission images from radiatively cooling Seyfert or protostellar jets, at least approximately these images would be representative of emission from a gas with radiative cooling proportional to $n^{2.5}T$, i.e., the jet density and poloidal magnetic field ($\sin \theta \approx 1$) are initially constant across the

jet and we assume that compressions of the magnetic field are comparable to compressions in the particle number density ($B \propto n$).

Patterns seen in the intensity image for simulation A are not readily identifiable with the prominent rectangular jet distortions apparent in the velocity cross sections although evidence of structure is apparent in the intensity image. The helical twisting indicated by the transverse velocities in Figure 2 produces only a barely discernible sinusoidal oscillation in the intensity image. The intensity image for simulation B readily reveals a sinusoidal oscillation that is identifiable with the helical motion of the jet indicated by the transverse velocities in Figure 2. Rotating elliptical distortion is not readily identifiable in the intensity image although some narrowing and broadening in the intensity image between $30R_0 - 50R_0$ is associated with this distortion. The elliptical distortion seen in the velocity cross sections in simulations C & D is apparent in the intensity images as an oscillation in jet width between axial distances of $10R_0 - 20R_0$. It is important to note that the oscillation in jet width in total intensity is not the result of axisymmetric pinching. The intensity images for simulations C & D show an unusual irregularly oscillating structure between $30R_0 - 40R_0$ which terminates as the axial velocity cross sections indicate development of a hollow jet. This intensity structure indicates that the jet beam develops an irregular helically twisted structure which terminates in a circumferential loop in simulation C, and which appears to loop back on itself slightly in simulation D at axial distances between $42R_0 - 43R_0$. In both these simulations the twist is in a counterclockwise sense when viewed downstream from the jet inlet (in the same sense as jet rotation). The polarization B-vectors overlaid on the intensity images are in general aligned with twisted structures in the intensity images, and the fractional polarization is relatively large except where the intensity image suggests cancellation of B-vectors by integration through twisted structures, e.g., note the much smaller B-vectors associated with the loop structure in simulations C & D at axial distances of $42R_0 - 43R_0$. The high fractional polarization and preferred orientation along the flow direction is a consequence of the strong ordered poloidal magnetic field component. Note that the more helical field in simulations C & D would still give polarization B-vectors initially aligned with the jet axis.

In the next section we investigate the types of structures that should develop in the transition between sub-Alfvénic and super-Alfvénic flow, compare theoretically predicted structures to those observed in the numerical simulations, and discuss the relationship between structure observed in the intensity images and the underlying flow dynamics.

3. Jet Structure

3.1. Stability Theory

The stability of an axially magnetized cylindrical jet with top hat profile residing in a uniform unmagnetized medium has been investigated in a number of papers, e.g., Ray 1981, Ferrari,

Trussoni, & Zaninetti 1981; Bodo et al. 1989, and we briefly review and extend the results here. It is assumed that the jet is a cylinder of radius R , having a uniform density, ρ_{jt} , a uniform internal axial magnetic field, B_{jt} , and a uniform velocity, u . Inclusion of a small non-uniform toroidal magnetic field component like that used in simulations A & B will not significantly modify results obtained from an analysis incorporating only axial magnetic fields, although we expect significant effects associated with the much stronger toroidal magnetic field used in simulations C & D, cf., Appl & Camenzind (1992), Appl (1996), RHCJ. The external medium is assumed to have a uniform density, ρ_{ex} , and to contain no magnetic field. The jet is established in static total pressure balance with the external medium where the total static uniform pressure is $p_{jt}^* \equiv p_{jt} + B_{jt}^2/8\pi = p_{ex}^* = p_{ex}$. The relatively slow jet expansion in the numerical simulations is not expected to significantly modify results based on a completely uniform external medium (Hardee 1984). In cylindrical geometry a random perturbation of ρ_1 , \mathbf{u}_1 , p_1 , and \mathbf{B}_1 to an initial equilibrium state ρ_0 , \mathbf{u}_0 , p_0 , and \mathbf{B}_0 can be considered to consist of Fourier components of the form

$$f_1(r, \phi, z) = f_1(r) \exp[i(kz \pm n\phi - \omega t)] \quad (1)$$

where flow is along the z -axis, and r is in the radial direction with the flow bounded by $r = R$. In cylindrical geometry k is the longitudinal wavenumber, n is an integer azimuthal wavenumber, for $n > 0$ the wavefronts are at an angle to the flow direction, the angle of the wavevector relative to the flow direction is $\theta = \tan(n/kR)$, and $+n$ and $-n$ refer to wave propagation in the clockwise and counterclockwise sense, respectively, when viewed outwards along the flow direction. In equation (1) $n = 0, 1, 2, 3, 4$, etc. correspond to pinching, helical, elliptical, triangular, rectangular, etc. normal mode distortions of the jet, respectively. Propagation and growth or damping of the Fourier components is described by a dispersion relation [cf., Hardee, Clarke, & Rosen (1997) eq.(A6), hereafter HCR].

In general, each normal mode, n , contains a single “surface” wave and multiple “body” wave solutions that satisfy the dispersion relation. The behavior of the solutions can be investigated analytically in the limit $\omega \rightarrow 0$.

In this limit the real part of the pinch mode ($n = 0$) surface wave solution becomes (Hardee 1995)

$$\frac{\omega}{k} \approx u \pm \left\{ \frac{1}{2} \left(V_A^2 + \frac{V_A^2 a_{jt}^2}{a_{ms}^2} \right) \pm \frac{1}{2} \left[\left(V_{A,jt}^2 + \frac{V_{A,jt}^2 a_{jt}^2}{a_{ms}^2} \right)^2 - 4 \frac{V_A^4 a_{jt}^2}{a_{ms}^2} \right]^{1/2} \right\}^{1/2}. \quad (2)$$

The imaginary part of the solution is vanishingly small in the low frequency limit. These solutions are related to fast (+) and slow (−) magnetosonic waves propagating with ($u+$) and against ($u-$) the jet flow speed u , but strongly modified by the jet-external medium interface. Numerical solution of the dispersion relation reveals that a growing solution is associated with the backwards moving (in the jet fluid reference frame) solution related to the slow magnetosonic wave and the pinch mode surface wave is unstable on sub-Alfvénic and super-Alfvénic jets.

When a jet is sub-Alfvénic the helical and higher order ($n > 0$) surface modes are stable

(Bodo et al. 1989; Hardee et al. 1992) and have an outwards moving purely real solution given by (e.g., Hardee & Clarke 1995)

$$\omega/k \approx u + V_A . \quad (3)$$

On the supermagnetosonic jet all higher order modes ($n > 0$) have surface wave solutions given by

$$\frac{\omega}{k} \approx \frac{\eta}{1+\eta} u \left\{ 1 \pm i \frac{[1 - (1+\eta)V_A^2/u^2]^{1/2}}{\eta^{1/2}} \right\} , \quad (4a)$$

or

$$\frac{ku}{\omega} \approx \frac{1}{1 - V_A^2/u^2} \left\{ 1 \pm i \frac{[1 - (1+\eta)V_A^2/u^2]^{1/2}}{\eta^{1/2}} \right\} , \quad (4b)$$

where the density ratio $\eta \equiv \rho_{jt}/\rho_{ex}$. Spatial growth corresponds to the minus sign in equation (4b) and a negative value for the imaginary part of the complex wavenumber. Note that in the dense jet limit, i.e., $\eta \rightarrow \infty$, equations (4a) and (4b) reduce to equation (3) with $\omega/k \approx u \pm V_A$, and thus the surface waves are related to Alfvén waves propagating with and against the jet flow speed but strongly modified by the jet-external medium interface. The unstable growing solution is associated with the backwards moving (in the jet fluid reference frame) wave. Equation (4a) indicates a surface wave speed in the observer frame, $(\omega/k)_{Real} \approx [\eta/(1+\eta)]u$, that is a strong function of the density ratio. When a jet is super-Alfvénic but transmagnetosonic the propagation speed and the growth rate at higher frequency can only be determined by numerical solution of the dispersion relation.

In the low frequency limit purely real body wave solutions are given by

$$kR \approx \frac{(n+2m-1/2)\pi/2}{[\{M_{ms}^2/[1 - (M_{ms}/M_{jt}M_A)^2]\} - 1]^{1/2}} \quad (5)$$

where $m \geq 1$ is an integer. However, unstable body wave solutions exist only when the denominator in equation (5) is real. This occurs if the jet speed is slightly below the slow magnetosonic speed, $u < v_{ms}^s$, and $u > a_{jt}V_A/(a_{jt}^2 + V_A^2)^{1/2}$, or if the jet speed is above the fast magnetosonic speed, $u > v_{ms}^f$, (Bodo et al. 1989; Hardee et al. 1992) where for wavevectors parallel to the axial magnetic field $v_{ms}^s = \text{Min}(a_{jt}, V_A)$ and $v_{ms}^f = \text{Max}(a_{jt}, V_A)$. These body wave solutions are growing at higher frequencies.

Displacements, $\xi(r, \phi, z)$, of jet fluid from an initial position (r, ϕ, z) are given by $\xi(r, \phi, z) = \xi(r) \exp[i(kz \pm n\phi - \omega t)]$ with the $\xi(r, \phi, z)$ given by equations (A9) in HCR, and where ω and k are normal mode solutions to the dispersion relation. In general $\xi(r)$ is complex and displacements, $\xi(r, \phi, z)$, the accompanying velocity perturbation, \mathbf{u}_1 , and the total pressure perturbation, $p_1^* \equiv p_1 + \mathbf{B}_1 \cdot \mathbf{B}_0 / 4\pi$, can be written in the form

$$\xi(r, \phi_s, z_s) = \mathbf{A}(r) e^{i\Delta(r)} \xi_{r,n}^s \exp[i(kz_s \pm n\phi_s - \omega t)] , \quad (6a)$$

$$\mathbf{u}_1 = -i(\omega - ku) \mathbf{A}(r) e^{i\Delta(r)} \xi_{r,n}^s \exp[i(kz_s \pm n\phi_s - \omega t)] , \quad (6b)$$

$$p_{1jt}^*(r) = B(r)e^{i\Delta_p(r)}\xi_{r,n}^s \exp[i(kz_s \pm n\phi_s - \omega t)] , \quad (6c)$$

where $\xi_{r,n}^s \equiv \xi_{r,n}(R)$, ϕ_s and z_s are now the radial displacement, azimuthal angle and axial position at the jet surface.

Fluid displacements are modified in amplitude and rotated in azimuthal angle or shifted along the jet axis relative to those at the jet surface by $\mathbf{A}(r)e^{i\Delta(r)}$ [see eqs.(A10) in HCR]. The accompanying velocity perturbation is given by $\mathbf{u}_1(r, \phi, z) = d\mathbf{\xi}/dt$, and the velocity perturbation is modified in amplitude and shifted in phase by the factor $-i(\omega - ku)\mathbf{A}(r)e^{i\Delta(r)}$.

In equation (6c) $B(r)e^{i\Delta_p(r)} = (\chi_{jt}/\beta_{jt})[J_n(\beta_{jt}r)/J'_n(\beta_{jt}R)]$ [cf., Hardee et al. (1998) eq. (14)] where J_n is a Bessel function, the prime denotes a derivative of the Bessel function with respect to its argument,

$$\beta_{jt} = \left[-k^2 + \frac{(\omega - ku)^4}{(\omega - ku)^2(a_{jt}^2 + V_A^2) - k^2 V_A^2 a_{jt}^2} \right]^{1/2} ,$$

and

$$\chi_{jt} = \rho_{jt}[(\omega - ku)^2 - k^2 V_A^2] .$$

If the dependence of the radial fluid displacement inside the jet on rotation in azimuth is small then the radial fluid displacement of a surface wave mode $n > 0$ is approximately given by $\xi_{r,n}(r) \approx \xi_{r,n}^s(r/R)^{n-1}$ (Hardee 1983). In general, simulations indicate a somewhat faster fall off in amplitude relative to the surface amplitude than that predicted by the analytical approximation (Hardee, Clarke, & Howell 1995). The accompanying velocity and pressure variations produced by higher order surface modes also are predicted to show a rapid decrease inwards. At a constant azimuth the body waves show a reversal in fluid displacement at null surfaces interior to the jet surface but we do not consider them further here as they are not important on the transmagnetosonic jet.

The stability of axially magnetized rotating supermagnetosonic jets has been investigated by Bodo et al. (1996). In general, Bodo et al. (1996) found that jet rotation provides some stabilization of the helical surface mode. The stabilizing effects of rotation are more pronounced at smaller longitudinal wavenumbers and diminish as the longitudinal wavenumber increases. The lesser effect at higher longitudinal wavenumbers is a consequence of the wavevector (the wavevector is at a large angle relative to the axial velocity for small longitudinal wavenumbers when $n > 0$) becoming more aligned with the axial velocity, hence reducing the effect of jet rotation on the velocity shear parallel to the wavevector. However, Bodo et al. (1996) also found that the helical mode corotating with jet rotation, $-n$ in eq. (1) for counterclockwise jet rotation, is less stabilized by rotation than the counter rotating helical mode, and that this effect is somewhat more pronounced for stronger magnetic fields. We expect that these results also apply to the higher order $n > 1$ surface modes which are essentially harmonics of the $n = 1$ helical mode. Thus, we expect modes destabilized at the Alfvén point to be corotating with the jet rotation if jet rotation dominates the precessional motion.

3.2. Theory and Simulations Compared

We have solved the dispersion relation numerically using root finding techniques over a wide range of frequencies for parameters appropriate to numerical simulations A & B for the surface and a representative sample of the body waves associated with the pinch ($n = 0$), helical ($n = 1$), elliptical ($n = 2$), triangular ($n = 3$) and rectangular ($n = 4$) modes. Results for parameters appropriate to simulation B in the sub-Alfvénic stable region at $z = 7R_0$, in the super-Alfvénic destabilization region at $z = 10.3R_0$, and in the transmagnetosonic region at $z = 18.1R_0$ are shown in Figure 7. Comparable results are found for parameters appropriate to simulation A. The predicted precessional perturbation frequency in the range $z = 7R_0 - 18.1R_0$ is $\omega R_{jt}/u \approx 0.11$ where $\omega R_0/a_{ex} = 0.5$, $R_{jt} > R_0$, and $u > 4a_{ex}$ reflect jet expansion and acceleration. In general, a jet with top hat profile is unstable to the surface pinching mode when sub-Alfvénic but is stable to body pinching and surface and body helical and higher order modes of jet distortion. Similar K-H instability behavior is predicted to occur in simulations A & B, but with the different axial location of the Alfvén point there are different growth rates and wavelengths predicted to accompany the perturbing frequency. Simulations C & D have a poloidal field component identical to that in simulation B, and differences between simulations C & D and the theoretically predicted unstable modes associated with simulation B will be the result of the stronger toroidal field, different jet thermal pressure profile, different axial location of the Alfvén point, and jet rotation.

The sub-Alfvénic solutions shown in Figure 7 indicate that equations (2) and (3) provide excellent estimates of the wave speed for pinch and higher order surface modes, respectively. Note that the theory indicates that a pinching perturbation propagates down the jet at less than the jet speed while a precessional perturbation propagates down the sub-Alfvénic jet at greater than the jet speed. Our simulation setup provides no source for a pinching perturbation other than minor symmetric disturbance as the jet enters the computational domain at the inlet, and we do not expect to see pinching even though the mode is unstable. For example, in simulation B the e-folding (growth) length of a pinch perturbation is $\ell_e > 5R_{jt}$, too long to provide sufficient amplification by the Alfvén point. We note that pinching or helical motion corresponding to the precessional frequency of $\omega R_{jt}/u \approx 0.11$ at $z = 7R_0$ in simulation B would result in pinching and helical wavelengths of $\lambda_p \approx 25R_{jt}$ and $\lambda_h \approx 115R_{jt}$, and the corresponding pinch e-folding length is $\ell_e \approx 100R_{jt}$ (note $R_{jt} \approx 1.1R_0$). The long helical wavelength and the absence of damping implies that the initial precessional motion is communicated nearly rigidly to the Alfvén point at $z \sim 8R_0$ in simulation B. In simulation A with $\langle \omega R_{jt}/u \rangle \approx 0.14$ between the origin and an Alfvén point at $\lesssim 35R_0$, the helical wavelength is comparably long, although somewhat shorter relative to the average jet radius, i.e., $\lambda_h \approx 90 \langle R_{jt} \rangle$. In simulation A there should be significant phase lag between precession at the origin and at the Alfvén point, and if the initial precession had significant amplitude the jet would exhibit noticeable curvature.

Immediately outside the Alfvén point the helical and higher order surface waves are rapidly growing, and, for example, helical e-folding lengths are $\ell_e \sim$ (A) $3R_{jt} \approx 4.5R_0$ and (B) $2R_{jt} \approx 2.2R_0$ at frequencies comparable to the precession frequency. The higher order surface

modes grow more rapidly. The longer predicted e-folding length for growth of helical motion in simulation A when compared to simulation B appears in the simulations as slower spatial development of transverse velocity oscillations in simulation A (see Fig. 2). We note that the wave speed associated with the surface modes at the precession frequency, $(\omega/k)_{Real} \approx [\eta/(1 + \eta)]u$, is no more than about 5% of the jet speed. In simulations A & B the jet speed on the super-Alfvénic jet is $u > v_{ms}^f = \text{Max}(a_{jt}, V_A)$ and the body waves are unstable. However, the body wave growth rates are found to be less than the pinch surface mode growth rate.

Beyond the Alfvén point the flow rapidly evolves into a “transmagnetosonic” regime where numerical solution of the dispersion relation shows that the helical and higher order surface modes have growth rates that are much larger than the growth rate of the surface pinch mode at all frequencies, and now also show a distinct maximum in the growth rates. The maximum growth rates are much larger and at much higher frequencies than the growth rates at the precession frequency. With the exception of the first pinch body wave which has a maximum growth rate comparable to that of the asymmetric surface wave modes, all body wave modes have growth rates that remain less than the growth rate of the pinch surface wave mode and should be unimportant. At axial distances beyond the Alfvén point simulations A & B remain in the “transmagnetosonic” regime with only modest changes to the growth rates and frequency–wavelength behavior. Thus, there is potential for very rapidly developing very short (relative to the jet radius) wavelength structure downstream of the Alfvén point.

The present results provide good evidence for coupling between the initial precession frequency, and the helical motion that develops downstream from the Alfvén point in simulations A & B even though the initial transverse perturbation is at the 1% level. To see that this is so we note that the observed helical wavelengths of (A) $7.6R_0$ and (B) $7.1R_0$ can be shown to correspond to (A) $\omega R_{jt}/u \approx 0.10$ & 0.22 at $z = 38.7R_0$ & $46.6R_0$, respectively, and (B) $\omega R_{jt}/u \approx 0.06$ & 0.14 at $z = 10.3R_0$ & $18.1R_0$, respectively. These locations bracket the region in which the precessional frequency of (A) $\omega R_{jt}/u \approx 0.17$ at $z = 40R_0$ and (B) $\omega R_{jt}/u \approx 0.11$ at $z = 15R_0$ can couple to a growing helical distortion with the observed wavelength. The rectangular surface mode that appears in the velocity cross sections in simulation A before the jet as a whole becomes super-Alfvénic provides evidence that surface modes can grow provided the jet has a sufficiently thick super-Alfvénic surface layer. The higher order surface wave modes that are readily apparent in the velocity cross sections in simulation B (see Fig. 4) do not have well defined wavelengths but are consistent with higher order modes having wavelengths appropriate to the precessional frequency.

In the “transmagnetosonic” region in simulations A & B the precession frequency is about an order of magnitude less than the frequency at which the growth rate is a maximum and the induced wavelengths are much longer than that associated with the maximum growth rate. The theory suggests that these “long” wavelength structures can achieve relatively large amplitudes with only modest pressure gradients because jet material does not need to move transverse to the flow direction at a large fraction of the magnetosonic speed, which is comparable to the flow speed.

In Figure 8 we show possible maximum helical, elliptical, triangular, and rectangular distortions appropriate to simulation B, and with wavelengths appropriate to the precessional frequency in the transmagnetosonic region. The maximum displacement is estimated from the distortions evident in velocity cross sections (Fig. 5) or from the transverse velocity oscillation (Fig. 2). The results shown in Figure 8 have used the dispersion relation solutions shown in Figure 7 in the transmagnetosonic region at $z = 18.1R_0$ and assumed a frequency of $\omega R_{jt}/u = 0.15$ to yield wavelengths representative of wavelengths in the transmagnetosonic region at larger axial distances. The wavelengths accompanying this frequency are $\lambda_1 = 5.6R_{jt}$, $\lambda_2 = 5.5R_{jt}$, $\lambda_3 = 6.2R_{jt}$, and $\lambda_4 = 8.7R_{jt}$ and the surface displacement amplitudes shown in Figure 8 are $\xi_{r,1}^s/R_{jt} = 0.3$, $\xi_{r,2}^s/R_{jt} = 0.3$, $\xi_{r,3}^s/R_{jt} = 0.2$, and $\xi_{r,4}^s/R_{jt} = 0.15$. These wavelengths and distortions are representative of wavelengths and maximum distortions seen in the transmagnetosonic region. Note that these wavelengths correspond to 360° , 180° , 120° , and 90° azimuthal rotations of the helical, elliptical, triangular, and rectangular distortions, respectively. The total pressure variation along with axial and transverse velocity components accompanying the distortions shown in Figure 8 are evaluated where these quantities show the largest fluctuation, at a radial location on the y -axis that is inside the maximally deflected jet surface.

The total pressure, axial velocity and transverse velocity components observed in simulation B along the z -axis and parallel to the z -axis at $x = 0.7R_0$ are shown in Figure 9. We see that the observed amplitudes of the total pressure fluctuations and the velocity fluctuations are comparable to the theoretical fluctuations expected to accompany the observed displacements. Along the z -axis pressure and axial velocity fluctuations are smaller than off the axis, and more regular transverse velocity oscillation is observed along the z -axis than off the axis. This is the expected result if multiple surface modes are operating in conjunction with a dominant helical mode. We note that no total pressure or velocity fluctuation is predicted to occur along the z -axis for elliptical and higher order modes, unless there is significant displacement of the jet beam off the z -axis associated with helical motion. On the other hand, significant pressure and velocity fluctuation produced by higher order modes should be observed off the z -axis even in the absence of significant helical displacement. While the elliptical surface mode produces significant displacements, pressures, and transverse motions in approximately the outer $3/4$ of the jet, the triangular and rectangular modes affect significantly only the outer $1/2$ and outer $1/3$ of the jet, respectively – examine the displacement contours in Figure 8 – and so only minimally effect transverse velocities measured on the z -axis unless helical motion displaces the jet off the z -axis by at least half the jet radius. Note that if multiple wave modes are operating, the total pressure and accompanying velocity fluctuations can be as large as a linear sum of the individual mode fluctuations. This fact allows us to immediately rule out, for example, a combination of large amplitude helical twist and large amplitude elliptical distortion in simulation B because the resulting transverse velocities would be much larger than those seen in simulation B. The relatively small total pressure variations predicted and observed to accompany the observed jet distortions and velocity fluctuations explain why little structure is seen in the intensity images in Figure 6, and why only sinusoidal oscillation associated with helical twisting and jet width fluctuation

associated with extreme elliptical distortion are evident.

The relatively strong toroidal magnetic field and accompanying large jet rotation in simulations C & D precludes a direct comparison to predictions made by linear stability theory although the normal modes of jet distortion and basic stability criteria do not change, i.e., the jet should be stable to asymmetric (helical etc.) normal modes provided the velocity shear parallel to the wavevector is less than the Alfvén speed parallel to the wavevector (Hardee et al. 1992). The large jet rotation that is present in simulations C & D will modify the velocity shear parallel to the wavevector of helical and higher order normal modes at small longitudinal wavenumbers. The transverse velocity vector plots in Figure 10 indicate that jet rotation has a significant effect on normal mode development. Recall that the jet rotation speed is on the order of 20% of the typical jet speed, and is more than an order of magnitude larger than the azimuthal motion induced by jet precession at the inlet. This large rotation speed is responsible for rapid development of the elliptical jet distortion that is apparent in the panel in Figure 10 at $z = 4R_0$, and that can be seen in the axial velocity cross sections (Fig. 5) and in the narrowing and broadening of the intensity images (Fig. 6) at somewhat larger axial distance. The elliptical distortion present in simulations C & D corotates with jet rotation as would be expected given that the jet rotation speed is much larger than the azimuthal speed introduced by the precessional motion at the inlet. The detail differences in spatial rotation of this elliptical distortion between simulations C & D (see Fig. 5) are the result of the precessional motion in simulation C that corotates with jet rotation, and in simulation D opposes jet rotation. Rapid appearance of the elliptical distortion in these two simulations by $z = 4R_0$ suggests that jet rotation has increased the velocity shear parallel to the elliptical distortion wavevector to super-Alfvénic levels in a suitably deep surface layer of the jet before the jet becomes super-Alfvénic on the jet axis at $z = z_A \sim$ (C) $6R_0$, and (D) $8R_0$.

At axial distances beyond about $20R_0$ jet motion is dominated by a helical twist but with an irregular wavelength that decreases up to the loop structure seen in the intensity images (Fig. 6) at an axial distance of $\sim 42R_0$. Beyond this distance the jets in simulations C & D show a longer wavelength helical distortion. Material at these larger distances is moving somewhat faster than the loop structure. Temporal animations of simulations C & D suggest that material at larger distance might move ahead of the loop structure at larger times, that the flow might no longer be continuous across the computational grid, and that the loop structure might develop into a slowly moving jet front. We note, however, that magnetic tension could prevent this development and much longer duration simulations are needed to address the long term flow behavior. The relationship between flow dynamics and the appearance of the loop in the intensity images is particularly interesting and is revealed in part in Figure 11 which shows contours of the axial velocity along with velocity vectors and contours of the flow angle with respect to the z -axis in a transverse slice plane at the location of the loop in simulation C. This figure shows that azimuthal velocities are up to a factor of two larger than axial velocities in the loop structure, and that there is some backwards axial flow at this location. The large azimuthal velocities combined with the lower axial velocities and study of animations show that the flow is counterclockwise and around

the loop structure seen in the intensity images in simulations C & D. However, the loop structure itself is moving downstream at about the velocity indicated in the axial velocity contours in Figure 11. Thus, the jet fluid flows azimuthally around the loop but does not flow through the loop in the downstream direction. In simulation C the bottom of the loop seen in the intensity image (lower left quadrant in Figure 11) is moving downstream more rapidly than the top portion of the loop. Further evolution of the loop structure in simulation C should result in a loop like that seen in simulation D where the bottom of the loop has overtaken the top and the jet appears to loop back on itself.

Previous work has indicated that development of the K-H instability in the linear growth regime leads to a slow linear growth in the entrained mass with subsequent rapid growth in the entrained mass in the non-linear regime followed by saturation in the amount of entrained mass (RHCJ). Elliptical jet distortion and subsequent filamentation proved to be particularly destructive to jet propagation through promotion of mass entrainment whereas higher order smaller amplitude surface distortions had a much lesser effect. These previous findings are reflected in the mass entrainment observed in simulations A & B. The lack of development of large scale distortion on the computational grid in simulation A, a result of longer growth lengths, appears directly related to the reduction in entrained mass relative to simulation B. Simulation B shows considerable development of the helical and elliptical distortions that previously have been observed to promote mass entrainment. Simulations C & D provide a more complex picture for the evolution of mixing of jet and external material. Previous work suggests that significant toroidal magnetic fields can reduce mass entrainment by suppressing filamentation of the jet beam. Our present results suggest that the strong toroidal field component in simulations C & D has prevented the early development of elliptical distortion seen in simulations C & D from entraining much more mass than is observed to be entrained in simulation B. Nevertheless, it is clear that the mass entrainment that occurs in simulations B, C & D and that is likely to occur in simulation A at larger spatial scales is not conducive to highly collimated “light” jet propagation to distances orders of magnitude beyond the Alfvén point.

4. Summary and Conclusion

We have shown that jets remain K-H stable to low order asymmetric normal modes, e.g., helical and elliptical modes, provided the jets are on average sub-Alfvénic. Apparently, higher order normal modes, e.g., the rectangular surface mode, can be unstable provided a jet has a sufficiently thick super-Alfvénic surface layer even when the jet is on average sub-Alfvénic. Jet rotation can be destabilizing when the addition of the rotational velocity to the axial velocity gives a total velocity shear parallel to the normal mode wavevector that is super-Alfvénic. The lower order normal modes rapidly destabilize when the jets become on average super-Alfvénic. We have observed transverse velocity fluctuations associated with helical twisting at up to twice the external sound speed, and half the jet’s fast magnetosonic speed in the super-Alfvénic and

transmagnetosonic regime. Observed jet distortions appear to be the result of K-H unstable helical, elliptical, triangular, and rectangular normal surface modes. No evidence for the accompanying body modes or for the pinch normal mode was evident in the simulations. These results are in agreement with a linear stability analysis that indicates rapid growth rates for the asymmetric normal surface modes on the super-Alfvénic and transmagnetosonic jet, but that also indicates growth rates over an order of magnitude lower for the accompanying body modes. We note that the pinch surface mode is predicted to be K-H unstable on the sub-Alfvénic and super-Alfvénic jet, albeit with relatively small growth rate, and the pinch first body mode is predicted to be K-H unstable on the super-Alfvénic jet with relatively high growth rate but the present simulations provide no appropriate perturbation.

The primarily poloidally magnetized jet simulations (A & B) indicate that an initial small amplitude precessional motion is effectively communicated down the jet to the Alfvén point. This motion is predicted to propagate at a wave speed $v_w \approx u + V_A$, although in the present simulations the induced amplitude and transverse velocity are too small, and the accompanying helical wavelength is too long to directly observe the predicted wave motion and helical twist in the sub-Alfvénic region. The precessional perturbation couples to growing jet distortions in the super-Alfvénic but transmagnetosonic regime which propagate very slowly relative to the jet speed for the “light”, $\rho_{jt}/\rho_{ex} \equiv \eta \ll 1$, poloidally magnetized jets in simulations A & B in accordance with a predicted wave (pattern) speed of $v_w \approx [\eta/(1 + \eta)]u$.

In simulations C & D with a significant toroidal magnetic field component, jet rotation accompanying the strong helical magnetic field is on the order of the external sound speed (about 25% of the jet speed at the inlet), overwhelms the initial precessional motion by over an order of magnitude, and the two simulations with opposite jet precession develop nearly identically. The jets in these simulations destabilize rapidly to elliptical jet distortion and subsequently to helical twisting of wavelength comparable to that in the poloidal magnetic field simulations A & B. The elliptical and helical distortions corotate with the jet rotation in accordance with expectations based on a linear stability analysis of the poloidally magnetized rotating jet (Bodo et al. 1996). The elliptical distortion in these two simulations appears before the jet becomes super-Alfvénic if only the axial jet velocity is considered. The presence of toroidal magnetic field appears to suppress the higher order normal modes that on poloidally magnetized jets are rapidly growing. This effect has also been observed in supermagnetosonic jet simulations containing a significant toroidal magnetic field (RHCJ).

No significant mass entrainment occurs in the sub-Alfvénic region in the poloidally magnetized simulations A & B but significant mass entrainment accompanies the development of helical twisting and elliptical distortion in the super-Alfvénic region. The large amplitude helical and elliptical jet distortions that accompany destabilization are associated with a total (magnetic plus thermal) pressure fluctuation at only the 10% – 20% level. Comparison between simulations and stability theory reveals that the distortions seen in the simulations are at relatively long wavelengths relative to the fastest growing wavelengths associated with the normal modes,

and that such “long” wavelength distortions can be induced by relatively small total pressure fluctuations. Since variation in the synchrotron emissivity is a function of the total pressure fluctuation, intensity images, e.g., simulation A, can show very little apparent structure even when jet cross sections and transverse velocity plots show readily identifiable albeit relatively small amplitude structure. Intensity images do reveal evidence for helical twisting related to the precession once the amplitude has become sufficiently large, e.g., simulation B, and some narrowing and broadening of the jet in the intensity image can be identified with elliptical distortion of the jet cross section. It is not possible to identify higher order jet distortions seen in jet cross sections with features in the intensity images.

In simulations C & D jet rotation induced by the helical magnetic field dominates the induced precessional motion at the inlet so in spite of the opposite precession the two jets develop similarly. The large jet rotation makes the jets unstable and effectively super-Alfvénic almost from the inlet, and significant mass entrainment begins earlier than would be expected based on the location of the Alfvén point on the jet axis. An apparent oscillation in jet width in the intensity image beginning near to the jet inlet is shown by jet cross section to be the result of an elliptical distortion, and not the result of a pinching distortion. Intensity images indicate an initial regular helical twist that develops into a complicated twisted structure which terminates in a loop in the intensity images. Axial velocity contours and transverse velocity vectors reveal a hollow jet with large azimuthal motion around the intensity loop but not through the loop axially as the loop moves outwards with the average outward flow speed. To our knowledge this is the first indication that jets can become hollow and develop an azimuthal circulation leading to the formation of a tight loop in an intensity image. Mass entrainment and slowing of the jet outflow associated with the loop structure may indicate the formation of a jet front.

The rapid onset of relatively short length scale jet distortion and accompanying mass entrainment that we observe in these simulations when they become super-Alfvénic but remain transmagnetosonic suggests the development of a plume like appearance at larger distances than we can simulate. Thus, the present simulations would be more appropriate to FR I type extragalactic jets whose appearance has been argued, cf., Bicknell (1994, 1995) to be the result of significant mass entrainment. The helically twisted structures that we do observe in the simulations would be on much shorter spatial length scales than those of twisted structures seen at parsec and kiloparsec length scales on extragalactic jets, e.g., M87 (Reid et al. 1989; Junor & Biretta 1995; Owen, Hardee & Cornwell 1989), unless helically twisted structures scale spatially with, say, the jet radius beyond the Alfvén point.

If magnetic jet acceleration and collimation schemes are to prove viable for the production of observed protostellar, and, in particular, FR II type extragalactic jets that propagate to distances orders of magnitude larger than the location of the Alfvén point, they must flow through the transmagnetosonic region much more stably than the jets in these simulations. We note that our present light jet simulations with relatively flat internal density, velocity and magnetic profiles are expected to be relatively unstable in both the linear and non-linear growth regimes (cf. HCR,

RHCJ). Additional stability both linearly and non-linearly may be achieved by different density, temperature, magnetic and velocity profiles, and through a higher jet density relative to the surrounding environment, or by the embedding of a jet in a surrounding wind. It is also possible that relativistic effects associated with jet and Alfvén speeds near to lightspeed will significantly modify the results and lead to a picture more consistent with extragalactic jets. Only future work designed to study relativistic effects, and to study the stability and mass entrainment properties of jet profiles consistent with those predicted to emerge from present magnetic acceleration and collimation schemes will answer these questions.

P. Hardee and A. Rosen acknowledge support from the National Science Foundation through grant AST-9318397 and AST-9802955 to the University of Alabama. The authors would also like to acknowledge David Clarke who has provided valuable support through development and maintenance of ZEUS-3D. The numerical work utilized the Cray C90 at the Pittsburgh Supercomputing Center through grant AST930010P.

REFERENCES

Apple, S. 1996, in ASP Conf. Series Vol. 100: Energy Transport in Radio Galaxies and Quasars, eds. P.E. Hardee, A.H. Bridle & A.Zensus, (San Francisco: ASP), 129

Appl, S., & Camenzind, M. 1992, A&A, 256, 354

Begelman, M.C. 1998, ApJ, 493, 291

Bicknell, G.V. 1994, ApJ, 422, 542

Bicknell, G.V. 1995, ApJS, 101, 29

Bodo, G., Massaglia, S., Rossi, P., Rosner, R., Malagoli, A., & Ferrari, A. 1995, A&A, 303, 281

Bodo, G., Rosner, R., Ferrari, A., & Knoblock, E. 1989, ApJ, 341, 631

Bodo, G., Rosner, R., Ferrari, A., & Knoblock, E. 1996, ApJ, 470, 797

Camenzind, M. 1997, in IAU Symp. 182: Herbig-Haro Flows and the Birth of Low Mass Stars, eds. B. Reipurth & C. Bertout, (Dordrecht: Kluwer), 241

Clarke, D.A. 1996, ApJ, 457, 291

Clarke, D.A., Norman, M.L., & Burns, J.O. 1989, ApJ, 342, 700

Ferrari, A., Trussoni, E., & Zaninetti, L. 1981, MNRAS, 196, 1051

Fiedler, R., & Jones, T.W. 1984, ApJ, 283, 532

Hardee, P.E. 1983, ApJ, 269, 94

Hardee, P.E. 1984, ApJ, 287, 523

Hardee, P.E. 1995, in Annals of the New York Academy of Sciences Vol. 773: Waves in Astrophysics, eds. J.H. Hunter & R.E. Wilson, 14

Hardee, P.E., & Clarke, D.A. 1995, ApJ, 449, 119

Hardee, P.E., Clarke, D.A., & Howell, D.A. 1995, ApJ, 441, 644

Hardee, P.E., Clarke, D.A., & Rosen, A. 1997, ApJ, 485, 533 (HCR)

Hardee, P.E., Cooper, M.L., Norman, M.L., & Stone, J.M. 1992, ApJ, 399, 478

Hardee, P.E., Rosen, A., Hughes, P.A., & Duncan, G.C. 1998, ApJ, 500, 599

Junor, W., & Biretta, J.A. 1995, AJ, 109, 500

Livio, M. 1997, in IAU Colloquium 163: Accretion Phenomena and Related Outflows, eds. D.T. Wickramasinghe, G.V. Bicknell & L. Ferrario, (San Francisco: ASP), 845

Meier, D.L., Payne, D.G., & Lind, K.R. 1996, in IAU Symp. 175: Extragalactic Radio Sources, eds. R. Eckers, C. Fanti & L. Padrielli, (Dordrecht: Kluwer), 433

Meier, D.L., Edgington, S., Godon, P., Payne, D.G., & Lind, K.R. 1997, Nature, 388, 350

Owen, F.N., Hardee, P.E., & Cornwell, T.J. 1989, ApJ, 340, 698

Ouyed, R., Pudritz, R.E., & Stone, J.M. 1997, *Nature*, 385, 409

Ouyed, R., & Pudritz, R.E. 1997, *Nature*, 482, 712

Ray, T.P. 1981, *MNRAS*, 196, 195

Reid, M.J., Biretta, J.A., Junor, W., Spencer, R., Muxlow, T.W.B., & Spencer, R.E. 1989, *ApJ*, 336, 112

Romanova, M.M., Ustyugova, G.V., Koldoba, A.V., Chechetkin, V.M., & Lovelace, R.V.E. 1997, *ApJ*, 482, 708

Rosen, A., Hardee, P.E., Clarke, D.A., & Johnson, A. 1999, *ApJ*, 510, in press (RHCJ)

Stone, J.M., Hawley, J.F., Evans, C.E., & Norman, M.L. 1992, *ApJ*, 388, 19

van Leer, B. 1977, *J.Comput.Phys.*, 23, 276

5. Figure Captions

Fig. 1.— Toroidal magnetic field profile (solid line) and thermal pressure profiles in simulation A (dotted line), simulation B (long dashed line) and simulations C & D (short dashed line) at the inlet. Jet thermal pressures are normalized to the pressure in the external medium at the inlet and jet toroidal magnetic field is normalized to the peak toroidal magnetic field.

Fig. 2.— Profiles of the velocity components scaled relative to the sound speed, a_{ex} , in the external medium along the z -axis at dynamical times τ_d = (A) 68, (B) 54, (C & D) 44 in the four simulations from simulation A (top row) to simulation D (bottom row). The arrows indicate the location of the Alfvén point on the jet axis.

Fig. 3.— Axial and transverse profiles in simulations A (top row) to D (bottom row) at the dynamical times used in Figure 2. In the first column the panels show values of the axial jet speed (solid line), jet sound speed (dotted line), Alfvén speed (long dashed line), and fast magnetosonic speed (dashed and dotted line) along the z -axis. In column two the panels show profiles of these speeds along the x -axis. Profiles along the x -axis are at locations z = (A) $38.7R_0$, (B) $18.1R_0$, (C) $14.0R_0$, and (D) $15.0R_0$ indicated by the vertical lines in the panels in column one. In columns three through five the panels show profiles along the x -axis of: (col.3) density, ρ , (solid line) and pressure, e , (dashed line), (col.4) temperature, e/ρ , and (col.5) total magnetic field, b , (solid line) and magnetic field components b_z (dotted line), b_y (dashed line), respectively. The density, pressure, and temperature are scaled to the density and $10/9 \times$ the pressure in the external medium at the inlet, and to $10/9 \times$ the temperature in the external medium, i.e., $\rho_{ex}(0)$, $1.11P_{ex}(0)$, and $1.11T_{ex}$, respectively. The speeds are scaled relative to the sound speed, a_{ex} , in the external medium. The magnetic field strength is found from $B = 1.291\sqrt{P_{ex}(0)} \times b$. Note that the vertical scales are not all identical.

Fig. 4.— Profiles of the average axial speed, $\langle v_z \rangle$, of jet plus entrained mass, and of the jet plus entrained mass per unit length, σ/σ_{jt} , in simulation A (solid line), B (dashed & dotted line), C (dotted line) and D (dashed line).

Fig. 5.— Axial velocity cross sections where dark indicates high values at axial distances from $6R_0$ to $60R_0$ in $6R_0$ increments in simulation A (top) to simulation D (bottom). The x -axis is in the vertical direction, the y -axis is in the horizontal direction and the flow direction (z -axis) is into the page. Each cross section has a dimension $4R_0 \times 4R_0$.

Fig. 6.— Intensity images of dimension $20R_0 \times 70R_0$ with fractional polarization B-vectors from simulations A (top) to D (bottom).

Fig. 7.— Solutions to the dispersion relation are shown as a function of angular frequency at three locations along the jet in simulation B. Surface pinch (P), helical (H), elliptical (E), triangular (T), and rectangular (R), and pinch 1st body (Pb₁) modes are shown. The real part of the wavenumber, k_R , is indicated by the dotted lines and the absolute value of the imaginary part of the wavenumber,

k_I , is indicated by the dashed lines. The precession frequency is $\omega R/u \approx 0.11$ at all three locations.

Fig. 8.— Displacement cross sections for helical, elliptical, triangular, and rectangular surface waves appropriate to simulation B along with 1D total pressure and velocity slices as a function of z in units of the jet radius, R . The 1D pressure and velocity slices are taken at positions on the y -axis indicated by the “ \times ” in the displacement cross sections. The dotted lines and the dashed lines indicate the x and y components of the velocity, respectively. Note that v_y is a radial motion of the fluid and v_x is an azimuthal motion of the fluid. The radial velocity lags the azimuthal velocity in phase, and the radial and azimuthal amplitudes can have different offsets about zero velocity.

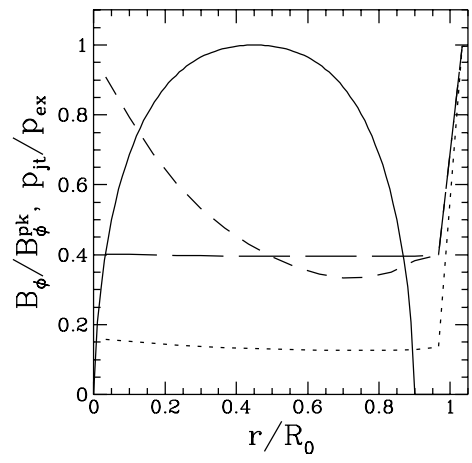
Fig. 9.— Total pressure, axial, and transverse velocity components from simulation B as a function of z in units of R_0 . The top panels are 1D slices along the z -axis and the bottom panels are 1D slices parallel to the z -axis at $x = 0.7R_0$. The dotted lines and the dashed lines indicate the x and y components of the transverse velocity, respectively. Note that these 1D slices are on the transverse axis orthogonal to that used for the theoretical 1D slices shown in Figure 8. Now v_x is a radial motion of the fluid and v_y is an azimuthal motion of the fluid. As in Figure 8 the radial velocity lags the azimuthal velocity in phase.

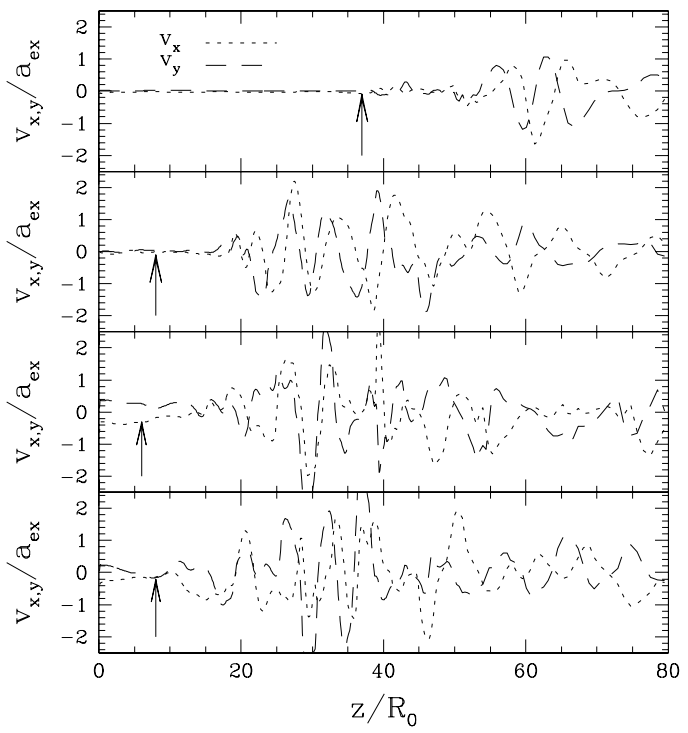
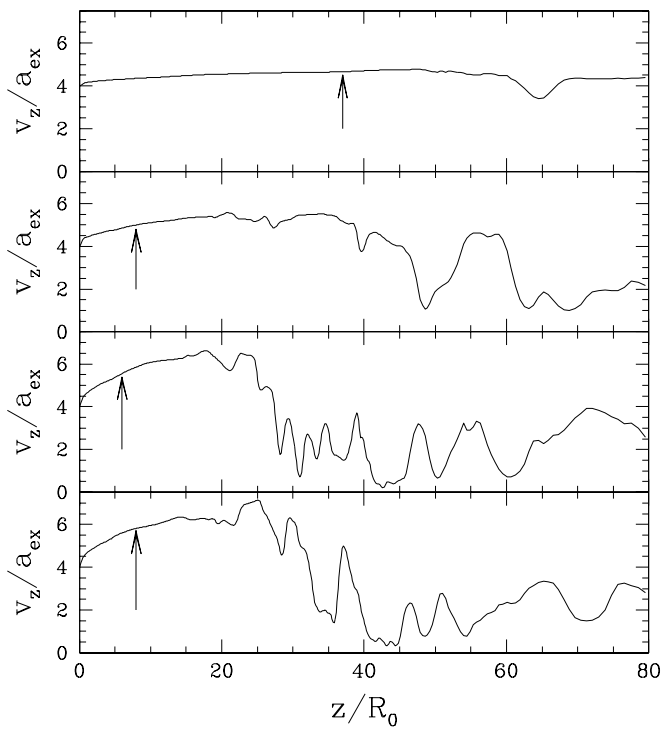
Fig. 10.— Transverse slices showing transverse velocity vectors in simulation C along the z -axis from $2R_0$ to $10R_0$ in $2R_0$ increments. Typical rotation speed is on the order of a_{ex} . Each cross section has a dimension $3R_0 \times 3R_0$, and a vector is shown for every other computational zone.

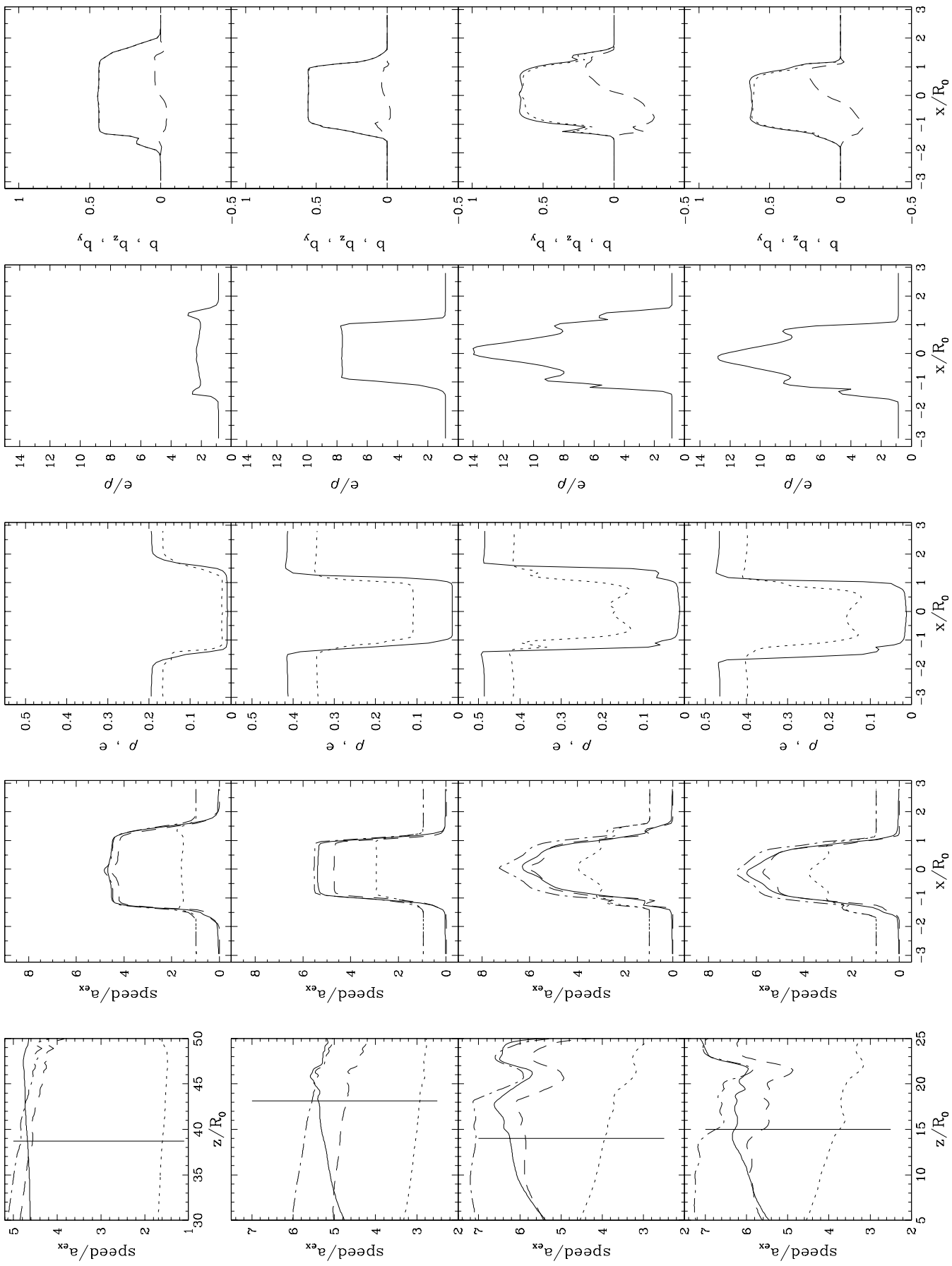
Fig. 11.— Contours of the axial velocity (first panel), transverse velocity vectors (second panel), and contours of the flow angle relative to the z -axis (third panel) in a transverse slice of dimension $8R_0 \times 8R_0$ from simulation C at an axial distance of $42R_0$. Contours in velocity are at intervals of $0.5a_{ex}$ and the bold arrow at the top of the velocity vector panel has a length of $4a_{ex}$. Note the dashed line contour that indicates negative (backwards) axial velocities on the order of $0.5a_{ex}$. The largest transverse velocities are about $5a_{ex}$.

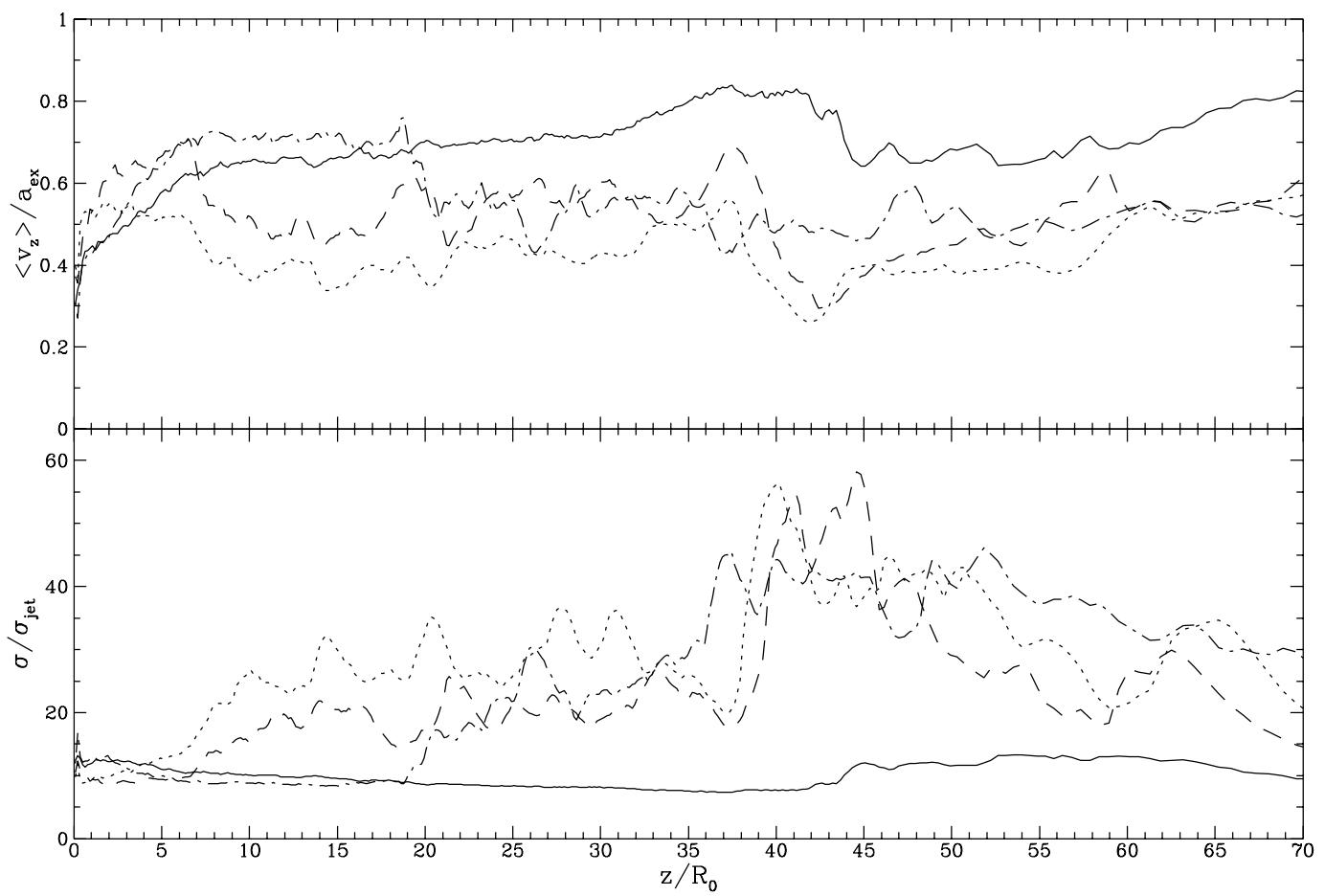
Table 1: Initial Conditions

Simulation	a_{jt}/a_{ex}	V_A/a_{ex}	a_{ms}/a_{ex}	$\langle M_{jt} \rangle$	$\langle M_A \rangle$	$\langle M_{ms} \rangle$	C_p	C_ϕ
A	2.32	6.00	6.43	1.85	0.66	0.62	6.567	0.050
B	3.71	5.00	6.23	1.08	0.80	0.64	1.526	0.004
C, D	5.40	5.00	7.36	1.01	0.77	0.61	1.526	0.298









This figure "hrfig5.jpg" is available in "jpg" format from:

<http://arxiv.org/ps/astro-ph/9906490v1>

This figure "hrfig6.jpg" is available in "jpg" format from:

<http://arxiv.org/ps/astro-ph/9906490v1>

